Nanoscale Advances

ROYAL SOCIETY OF CHEMISTRY

PAPER

View Article Online
View Journal | View Issue

Cite this: *Nanoscale Adv.*, 2021, **3**, 4286

Linewidth narrowing of aluminum breathing plasmon resonances in Bragg grating decorated nanodisks†

Xiaomin Zhao,‡[a] Chenglin Du,‡[a] Rong Leng,‡[a] Li Li,[a] Weiwei Luo,[a] Wei Wu,[a] Yinxiao Xiang,[a] Mengxin Ren,[ab] Xinzheng Zhang,[ab] Wei Cai *[ab] and Jingjun Xu*[ab]

Received 11th March 2021
Accepted 1st June 2021

DOI: 10.1039/d1na00184a

rsc.li/nanoscale-advances

Plasmon resonances with high-quality are of great importance in light emission control and light–matter interactions. Nevertheless, inherent ohmic and radiative losses usually hinder the plasmon performance of metallic nanostructures, especially for aluminum (Al). Here we demonstrate a Bragg grating decorated nanodisk to narrow the linewidth of breathing plasmon resonances compared with a commensurate nanodisk. Two kinds of plasmon resonant modes and the corresponding mode patterns are investigated in cathodoluminescence (CL) depending on the different electron bombardment positions, and the experimental results agree well with full wave electromagnetic simulations. Linewidth narrowing can be clearly understood using an approximated magnetic dipole model. Our results suggest a feasible mechanism for linewidth narrowing of plasmon resonances as well as pave the way for in-depth analysis and potential applications of Al plasmon systems.

1. Introduction

Surface plasmon resonances, collective electron oscillations in metallic nanostructures, can concentrate light in a sub-wavelength scale and efficiently enhance the optical near-field.[1] The unique properties of metallic nanostructures led to their extensive application in diverse fields of nanophotonics, including nanoscale light sources,[2] photovoltaics,[3] and optical sensors.[4,5] In the past few decades, noble metals such as gold and silver were widely used materials for plasmon research studies. However, the inherent optical properties limit their applications in ultraviolet (UV) spectral ranges and their high cost hinders their industrialization as well. Recently, aluminum (Al) has attracted much attention thanks to its unique plasmon properties from the visible to the UV spectral ranges,[6–10] which has been demonstrated in colorimetric sensing,[11] enhanced fluorescence,[12] enhanced Raman spectroscopy,[13] and nonlinear plasmonics.[14] However, the common drawback in Al plasmon resonance is the broad linewidth originating from the high imaginary parts of dielectric functions,[15–17] which inhibits its use for strong light–matter interactions. As a result, realization of a plasmon resonance with a narrow linewidth in Al nanostructures is a key problem to be resolved, as this will facilitate the design of nanostructures that interact more efficiently with light.

Until now, linewidth narrowing of plasmon resonances has been explored relying on different strategies. First of all, lowering of losses by improving the quality of the metal should be adopted, for example, high purity synthesized Al nanocrystals[18] and single-crystal Al show a better plasmon response.[19,20] In addition, plasmon coupling between several isolated nanostructures, in which hybridized modes can be obtained and lead to narrow linewidths, such as profound linewidth narrowing has been realized in Al nanoparticle-film systems[6] and ring-disk nanocavities.[21] Moreover, the collective resonance effect, such as surface lattice resonance can also be adopted, which has been demonstrated in metallic nanoparticles array.[22] More recently, the bound state in continuum[23] was found to be another possible solution to realize a narrow linewidth; however, it is still difficult to realize in a plasmonic system.

In this study, relying on the plasmon coupling effect, Bragg grating decorated nanodisks (BGDNs)[24–26] are adopted and linewidth narrowing of plasmon resonances is shown compared with that of a commensurate Al nanodisk. The experiments are performed in a spatially and spectrally resolved cathodoluminescence (CL) system and numerical simulations are carried out by using finite-difference time-domain (FDTD) methods. The results show that a fourfold linewidth narrowing is achieved in the experiment. Also, two kinds of plasmon resonances, namely breathing and edge modes, are excited and

[a]*The Key Laboratory of Weak-Light Nonlinear Photonics, Ministry of Education, School of Physics, TEDA Institute of Applied Physics, Nankai University, Tianjin 300457, China. E-mail: weicai@nankai.edu.cn; jjxu@nankai.edu.cn*

[b]*Collaborative Innovation Center of Extreme Optics, Shanxi University, Taiyuan, Shanxi 030006, People's Republic of China*

† Electronic supplementary information (ESI) available. See DOI: 10.1039/d1na00184a

‡ Contributed equally to this work.

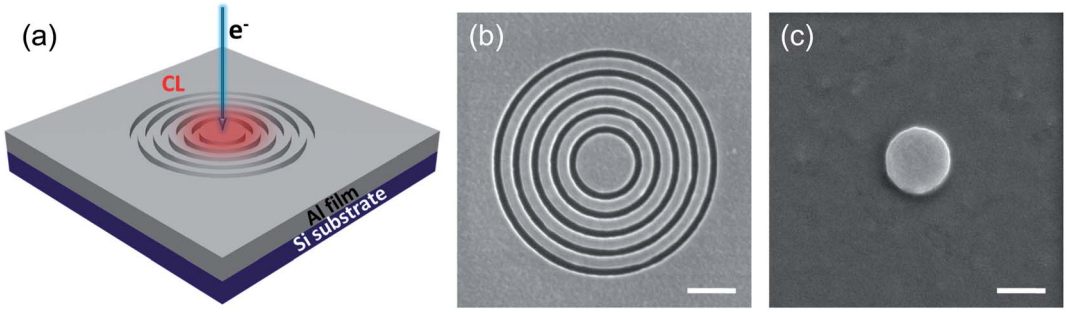

Fig. 1 (a) Schematic illustration of the Al Bragg grating decorated nanodisks (BGDNs). A 300 nm thick Al film was evaporated on a silicon substrate, and the depth of the BGDN is 70 nm, fabricated by using focused ion beam (FIB) milling. The structure is excited by electrons and then cathodoluminescence (CL) spectra are measured. (b) and (c) SEM images of the Al BGDN and the isolated Al nanodisk. The scale bars are 500 nm.

imaged depending on the different electron beam positions. Moreover, the linewidth narrowing is further understood by an equivalent magnetic dipole model. On the basis of the obtained results, we demonstrate that Al BGDN is a simple and efficient plasmonic system for narrowing the linewidth and increasing the quality factor of plasmon resonances.

2. Experiment and results

The schematic illustration of the Al BGDN and electron beam excitation is presented in Fig. 1(a). The experiments are performed in a CL system, in which an electron beam bombards the sample to excite the plasmon resonances. It is well known that CL has the versatility to probe the radiative photonic local density and map the plasmon modes in the near field at a deep subwavelength scale.[27–35] Pioneering research studies on Al plasmons have been implemented by CL[20,31,36–38] or electron energy-loss spectroscopy (EELS)[39–41] techniques. Here, our designed BGDN consists of a central disk and four concentric rings were fabricated using a focused ion beam (FIB) milling on a 300 nm thick Al film evaporated on a silicon wafer with a depth of 70 nm. Fig. 1(b) shows the scanning electron microscope (SEM) image of the nanostructure. The diameter of the central disk is 600 nm and the period of the grating is 200 nm with a duty cycle of 0.55. For reference, an isolated Al nanodisk with the same diameter of 600 nm was also fabricated on the same substrate and its SEM image is shown in Fig. 1(c).

In the CL experiment, a 30 keV electron beam is used to excite the plasmon modes of the nanostructures shown in Fig. 1(b) and (c) respectively. As a contrast, a vertical electric dipole is used to imitate the electron beam and the Purcell factor is calculated in FDTD simulations (Methods). First, when the electron beam is incident at the center of the Al BGDN, a distinct CL peak is observed around 500 nm as shown in Fig. 2(a). However, in the contrast experiment for the isolated Al nanodisk, there is a peak around 500 nm as well, but showing a very broad linewidth. Both peaks are come from to the same plasmon resonances in the central disk and the near field images are shown in the insets in Fig. 2(a), where the images were obtained by scanning the electron beams on the sample in real-space. The simulated spectra and images of the corresponding structures are plotted in Fig. 2(b) and show good agreement with the experimental ones. Furthermore, the Q factors of the plasmon peaks can be extracted by Lorentz fit (green lines in Fig. 2). As expected, a higher Q factor of 6.9 is realized in the Al BGDN compared with the isolated Al nanodisk ($Q = 1.7$) demonstrating a fourfold linewidth narrowing. At the same time, the simulated results ($Q = 7.9$ for Al BGDN and $Q = 3.2$ for isolated Al nanodisk) are verified well by the experiment results. Besides, the theoretical calculated near-fields of the Al

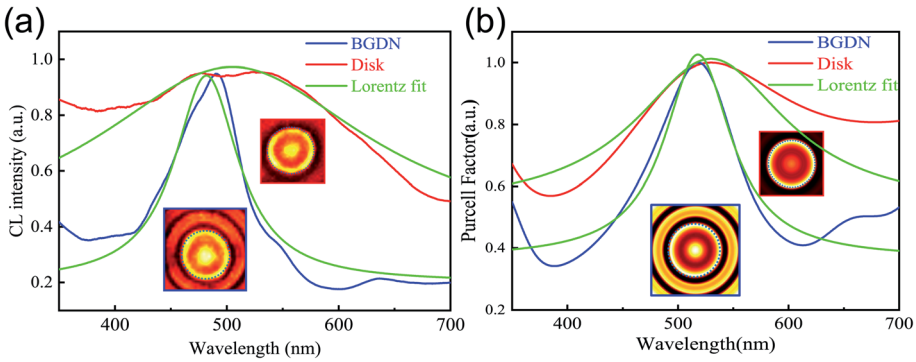

Fig. 2 (a) Measured and (b) calculated CL spectra of an isolated Al nanodisk (red) and an Al BGDN (blue) shown in Fig. 1(b) and (c). The corresponding Lorentzian line shape fitting curves are also plotted as green lines. The insets show the CL images at resonant wavelengths respectively.

BGDN and isolated disk (insets in Fig. 2(b)) are perfectly revealed by CL near-field scanning (insets in Fig. 2(a)). Further, the narrowing effect of the Bragg grating was found to be tunable by manipulating the distance between the disk and the first ring and can be applied not only to the breathing mode but also to other plasmon modes, such as the quadrupole mode and hexapole mode (see the ESI†).

Next, to understand the plasmon modes in the Al BGDN, the dependence of the electron beam excitation position and the spatial distributions of the plasmon modes are investigated in detail. Relying on the high spatial resolution of CL spectroscopy, different local excitation positions can be realized easily. Fig. 3(a) and (b) show experimental and simulated CL spectra, and the corresponding schematic illustrations of the excitation positions are depicted as well. When the beam position is at the disk center of the Al BGDN, only one resonance peak labeled as C appears in the 350–700 nm spectral range. On the other side, if the electron is incident on the disk edge, three resonance peaks A, B and D are observed. Simulated CL spectra agree well with the experimental ones while the slight differences are attributed to the deviation of the geometry and dielectric function of Al[42] between experiments and models. Moreover, due to the limited detection range of our experimental system, we cannot detect the CL signal in the near infrared region, though dipolar modes are expected to appear in this range (see the ESI†). Experimental CL maps are performed at the

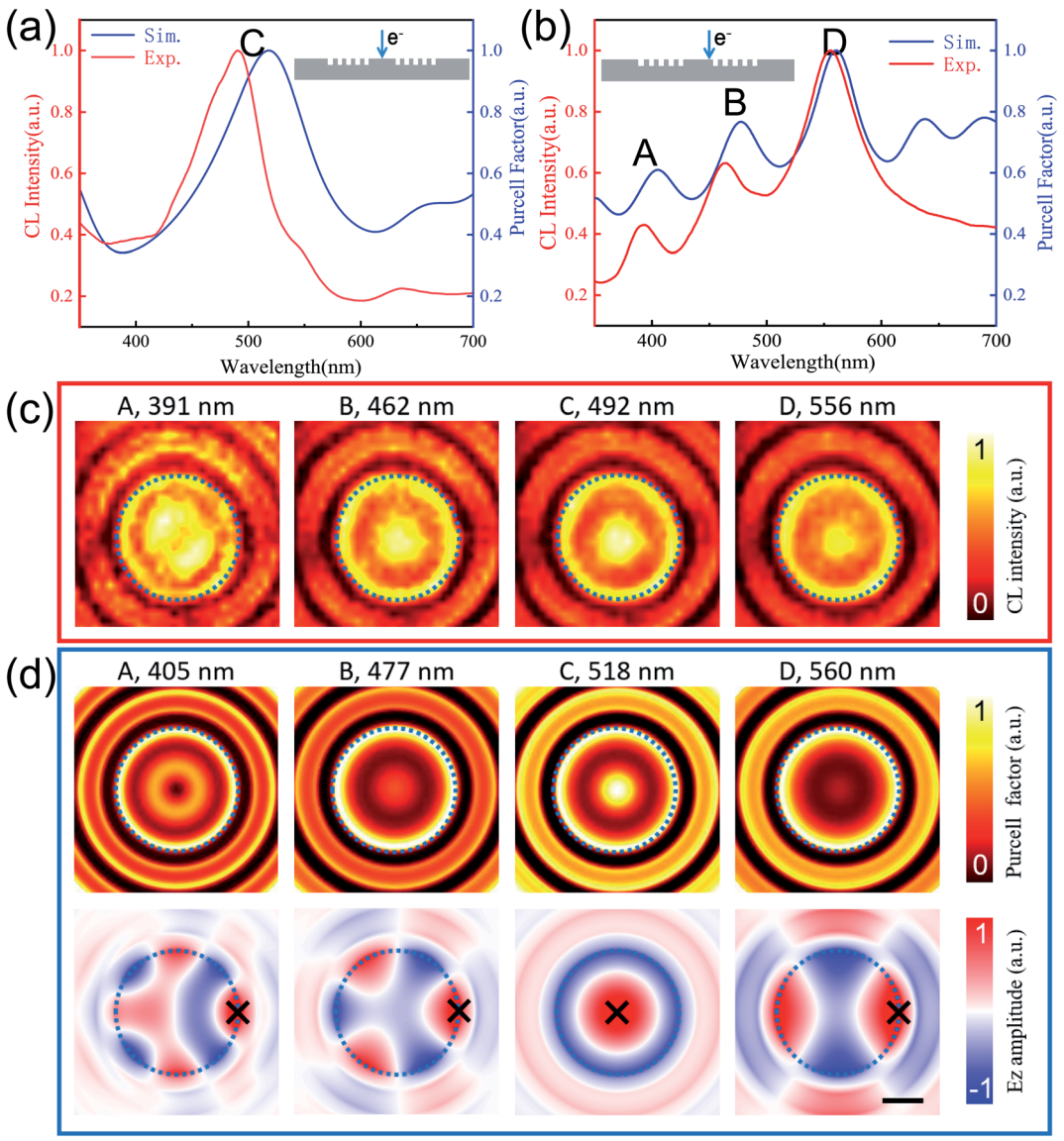

Fig. 3 Experimental (red) and simulated (blue) CL spectra from the disk center (a) and edge (b) excitation respectively. The insets show the corresponding schematic illustrations of the excitation positions. The resonance peaks for comparison with the CL maps in (c) and (d) are marked with letters A–D. (c) Experimental CL maps extracted at the resonant wavelengths (391, 462, 492 and 556 nm) observed in panels (a) and (b). (d) Upper panel: simulated CL maps for the experimental geometry at resonant wavelengths (405, 477, 518 and 560 nm). Lower panel: simulated E_z field distributions generated by assuming the fixed electron beam positions marked by the black crosses. The black dashed lines indicate the edges of the central disks. All scale bars are 200 nm.

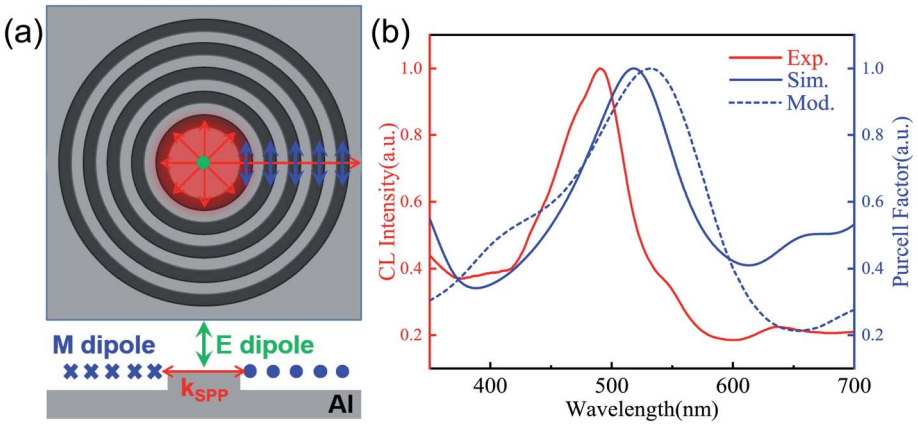

Fig. 4 (a) Schematic illustration of the magnetic dipole model (top and side views). The green dot (arrow in side view) represents the electric dipole position and orientation for plasmon excitation, the red arrows represent the direction of plasmon propagation, and the blue arrows (dots in side view) represent the magnetic dipole positions and orientations. (b) Comparison of the experimental (red line) and simulated (blue line) CL spectra for Al BGDN nanostructures with the simulated results using a magnetic dipole model (blue dashed line).

respective peak wavelengths with a 20 nm bandwidth and presented in Fig. 3(c). The simulated CL maps in Fig. 3(d) (upper panel) agree well with the experimental results apart from the mode A, and the slight inconsistency of mode A may come from the inhomogeneous surface of the structure in the experiment. For the modes B, C, and D, both a bright ring around the edge and a bright spot at the center are observed. Moreover, the central hotspot is brighter in mode C than in the others. It is worth noting that mode A shows a dark spot instead of a bright one at the center of the disk. These CL intensity distributions correspond to the localized surface plasmon resonances and to a radiative photonic local density of states projected along the direction of the electron trajectory physically.[43] However, due to the azimuthal symmetry of the Al BGDN, the plasmon modes still cannot be assigned accurately.

To address this issue, the E_z field distributions perpendicular to the surface of the disk for the simulated resonance wavelengths assuming the fixed position of the electron beam are calculated. As shown in Fig. 3(d) (lower panel), the black crosses represent the electron beam positions. The plasmon modes can be assigned with azimuthal and radius mode numbers (m, n). From the figure, it is clear that the plasmon modes A, B, and D are demonstrated to be octupole (4, 0), hexapole (3, 0), and quadrupole (2, 0) respectively when the beam position is close to the edge. Furthermore, the previous mentioned central dark spot for mode A can be understood by a π phase jump of the electrical field at the center of the disk, which is clearly demonstrated by the E_z amplitude of the mode. For the plasmon mode A, there was no charge at the center of the disk. According to rotational symmetry, the Purcell factor plot is dark at the center of the disk. At the same time, the plasmon mode C proves to be a lower order mode (0, 1), which is a breathing mode rather than an edge one due to the rotational symmetry of the excitation and nanostructure. For each plasmon mode in the hybrid structure, the outer ring structure shows different near-field distributions, suggesting that the narrowing effect comes from the plasmon interaction between specific modes.

Further, in order to ascertain the origin of the linewidth narrowing of the breathing mode (0, 1) in the Al BGDN, an equivalent magnetic dipole model is used to analyze the behavior of plasmons in the Al BGDN.[44] It is known that surface plasmons are a transverse magnetic (TM) wave and induce a magnetic dipole resonance when propagating to a groove. As a result, in the model, the BGDN is described as a central nanodisk and a series of in-plane magnetic dipoles, in which the contributions for Bragg grating are represented with the magnetic dipoles in the grooves. The orientation of the dipoles is parallel to the TM field of the incoming surface plasmon wave as shown in Fig. 4(a). As before, a vertical electric dipole is used to excite the plasmon mode in the central disk but each outer ring is replaced by 8 horizontal magnetic dipoles distributed evenly along the circumference at the groove center (details in Methods and the ESI†). Fig. 4(b) presents the results of the comparison between the experimental and simulated CL spectra of the Al BGDN and the simulated spectrum using the equivalent magnetic dipole model. Obviously, the spectrum obtained using the equivalent magnetic dipole model is in good agreement with the simulated ones, although the linewidth and peak position have a slight difference, demonstrating the validity of the model as well as the origin of the effective linewidth narrowing for the breathing mode in the Al BGDN.

3. Conclusion

In summary, we use CL spectroscopy to excite and image the plasmon modes of an Al BGDN nanostructure. The obtained experimental results show that the linewidth of breathing plasmon resonance is narrowed fourfold compared to that of an isolated disk without circular Bragg grating. The experimental results agree well with the simulated ones carried out by using FDTD methods. Furthermore, the physical mechanism behind the narrowing is clearly explained by the equivalent magnetic

dipole model. Our work provides useful insight into the study on the linewidth of the plasmon resonance of Al nanostructures. We hope that the results of this study will be useful to achieve strong light–matter interactions in the UV region, such as large luminescence enhancement of quantum dots coupled to Al nanostructures.

4. Methods

The Al BGDN structures used in this study were fabricated as follows. First a 300 nm thick Al film was deposited onto a crystalline silicon substrate by electron beam evaporation. The film was evaporated at a rate of 0.3 nm s^{-1} under a pressure of 3×10^{-6} torr. Then the 70 nm depth BGDN structure was carved using a focused ion beam (FIB) milling method. A 30 keV, 7.7 pA Ga^{+} beam in a FEI Helios NanoLab 600i system was used to obtain the sharply defined boundaries.

The CL experiments were performed as follows. The sample was excited by a 30 keV, 11 nA electron beam in a SEM. A parabolic mirror placed above the sample collected the light emitted from the sample and guided it to a spectrometer in which the light was spectrally resolved and then detected using a liquid-nitrogen-cooled charge-coupled device array, and the spectra were recorded in the 350–700 nm spectral range. The measured spectra were corrected for system response by measuring the transition radiation spectrum for Al and comparing that to theory. A dwell time of 5 s was used for the CL spectra and 0.5 s for the CL maps.

Commercial software (FDTD solutions, Lumerical) was used for the full wave electromagnetic simulation of the optical properties of the Al nanostructures. The following parameters were employed in the numerical simulations. The dielectric functions for Al were derived by fitting the Drude model to the permittivity data given by Palik.[42] A 5 nm mesh grid was used for discretization in each axis and 8 perfect matching layers (PMLs) were employed for the boundaries. An electric dipole polarized along the z direction and positioned 15 nm above the disk center was used to mimic the electron beam excitation. For the magnetic dipole model, the magnetic dipole amplitude is given by $e^{-r\,\mathrm{Im}(k_{SPP})}/\sqrt{r}$, where r represents the distance between the magnetic dipole and electric dipole and $\mathrm{Im}(k_{SPP})$ represents the imaginary part of the SPP wave vector at the interface between Al and air. The propagation of SPP was imitated by excitation of the magnetic dipoles along radial directions with different time offsets t.

Conflicts of interest

There is no conflicts to declare.

Acknowledgements

This work was supported by the Guangdong Major Project of Basic and Applied Basic Research (2020B0301030009), the Program for the National Key R&D Program of China (2017YFA0305100 and 2017YFA0303800), the National Natural Science Foundation of China (91750204, 12074200, 11774185, 61775106, and 92050114), the Changjiang Scholars and Innovative Research Team in University (IRT13_R29), the 111 Project (B07013), the Tianjin Natural Science Foundation (18JCQNJC02100), and the Fundamental Research Funds for the Central Universities.

References

1 W. L. Barnes, A. Dereux and T. W. Ebbesen, *Nat. Mater.*, 2003, **424**, 824–830.
2 K. Okamoto, I. Niki, A. Shvartser, Y. Narukawa, T. Mukai and A. Scherer, *Nat. Mater.*, 2004, **3**, 601.
3 H. A. Atwater and A. Polman, *Nat. Mater.*, 2010, **9**, 205.
4 J. N. Anker, W. P. Hall, O. Lyandres, N. C. Shah, J. Zhao and R. P. Van Duyne, *Nat. Mater.*, 2008, **7**, 442.
5 S. Lal, S. Link and N. J. Halas, *Nat. Photonics*, 2007, **1**, 641.
6 A. Sobhani, A. Manjavacas, Y. Cao, M. J. McClain, F. J. García de Abajo, P. Nordlander and N. J. Halas, *Nano Lett.*, 2015, **15**, 6946–6951.
7 M. W. Knight, N. S. King, L. Liu, H. O. Everitt, P. Nordlander and N. J. Halas, *ACS Nano*, 2014, **8**, 834–840.
8 G. Maidecchi, G. Gonella, R. Proietti Zaccaria, R. Moroni, L. Anghinolfi, A. Giglia, S. Nannarone, L. Mattera, H.-L. Dai, M. Canepa and F. Bisio, *ACS Nano*, 2013, **7**, 5834–5841.
9 A. Taguchi, Y. Saito, K. Watanabe, S. Yijian and S. Kawata, *Appl. Phys. Lett.*, 2012, **101**, 081110.
10 C. Langhammer, M. Schwind, B. Kasemo and I. Zorić, *Nano Lett.*, 2008, **8**, 1461–1471.
11 N. S. King, L. Liu, X. Yang, B. Cerjan, H. O. Everitt, P. Nordlander and N. J. Halas, *ACS Nano*, 2015, **9**, 10628–10636.
12 M. H. Chowdhury, K. Ray, S. K. Gray, J. Pond and J. R. Lakowicz, *Anal. Chem.*, 2009, **81**, 1397–1403.
13 S. K. Jha, Z. Ahmed, M. Agio, Y. Ekinci and J. F. Löffler, *J. Am. Chem. Soc.*, 2012, **134**, 1966–1969.
14 M. Castro-Lopez, D. Brinks, R. Sapienza and N. F. van Hulst, *Nano Lett.*, 2011, **11**, 4674–4678.
15 G. H. Chan, J. Zhao, G. C. Schatz and R. P. V. Duyne, *J. Phys. Chem. C*, 2008, **112**, 13958–13963.
16 B. R. Michael and C. S. George, *J. Phys. D: Appl. Phys.*, 2015, **48**, 184004.
17 I. Zorić, M. Zäch, B. Kasemo and C. Langhammer, *ACS Nano*, 2011, **5**, 2535–2546.
18 M. J. McClain, A. E. Schlather, E. Ringe, N. S. King, L. Liu, A. Manjavacas, M. W. Knight, I. Kumar, K. H. Whitmire, H. O. Everitt, P. Nordlander and N. J. Halas, *Nano Lett.*, 2015, **15**, 2751–2755.
19 H. W. Liu, F. C. Lin, S. W. Lin, J. Y. Wu, B. T. Chou, K. J. Lai, S. D. Lin and J. S. Huang, *ACS Nano*, 2015, **9**, 3875–3886.
20 C. Du, W. Cai, W. Wu, L. Li, Y. Xiang, M. Ren, X. Zhang and J. Xu, *ACS Photonics*, 2018, **5**, 2983–2989.
21 F. Hao, P. Nordlander, M. T. Burnett and S. A. Maier, *Phys. Rev. B: Condens. Matter Mater. Phys.*, 2007, **76**, 245417.
22 W. Zhou and T. W. Odom, *Nat. Nanotechnol.*, 2011, **6**, 423.
23 C. W. Hsu, B. Zhen, A. D. Stone, J. D. Joannopoulos and M. Soljačić, *Nat. Rev. Mater.*, 2016, **1**, 16048.

24 M. Y. Su and R. P. Mirin, *Appl. Phys. Lett.*, 2006, **89**, 033105.
25 C. I. Osorio, T. Coenen, B. J. M. Brenny, A. Polman and A. F. Koenderink, *ACS Photonics*, 2016, **3**, 147–154.
26 N. M. H. Duong, Z.-Q. Xu, M. Kianinia, R. Su, Z. Liu, S. Kim, C. Bradac, T. T. Tran, Y. Wan, L.-J. Li, A. Solntsev, J. Liu and I. Aharonovich, *ACS Photonics*, 2018, **5**(10), 3950–3955.
27 W. Cai, R. Sainidou, J. Xu, A. Polman and F. J. Garcia de Abajo, *Nano Lett.*, 2009, **9**, 1176–1181.
28 E. J. R. Vesseur, R. de Waele, M. Kuttge and A. Polman, *Nano Lett.*, 2007, **7**, 2843–2846.
29 J. K. Day, N. Large, P. Nordlander and N. J. Halas, *Nano Lett.*, 2015, **15**, 1324–1330.
30 B. J. M. Brenny, D. M. Beggs, R. E. C. van der Wel, L. Kuipers and A. Polman, *ACS Photonics*, 2016, **3**, 2112–2121.
31 M. Jeannin, N. Rochat, K. Kheng and G. Nogues, *Opt. Express*, 2017, **25**, 5488–5500.
32 T. Han, S. Zu, Z. Li, M. Jiang, X. Zhu and Z. Fang, *Nano Lett.*, 2018, **18**, 567–572.
33 N. Kawasaki, S. Meuret, R. Weil, H. Lourenço-Martins, O. Stéphan and M. Kociak, *ACS Photonics*, 2016, **3**, 1654–1661.
34 A. C. Atre, B. J. M. Brenny, T. Coenen, A. García-Etxarri, A. Polman and J. A. Dionne, *Nat. Nanotechnol.*, 2015, **10**, 429.
35 V. Myroshnychenko, J. Nelayah, G. Adamo, N. Geuquet, J. Rodríguez-Fernández, I. Pastoriza-Santos, K. F. MacDonald, L. Henrard, L. M. Liz-Marzán, N. I. Zheludev, M. Kociak and F. J. García de Abajo, *Nano Lett.*, 2012, **12**, 4172–4180.
36 M. J. McClain, A. E. Schlather, E. Ringe, N. S. King, L. Liu, A. Manjavacas, M. W. Knight, I. Kumar, K. H. Whitmire, H. O. Everitt, P. Nordlander and N. J. Halas, *Nano Lett.*, 2015, **15**, 2751–2755.
37 M. W. Knight, L. F. Liu, Y. M. Wang, L. Brown, S. Mukherjee, N. S. King, H. O. Everitt, P. Nordlander and N. J. Halas, *Nano Lett.*, 2012, **12**, 6000–6004.
38 L. Li, W. Cai, C. Du, Z. Guan, Y. Xiang, Z. Ma, W. Wu, M. Ren, X. Zhang, A. Tang and J. Xu, *Nanoscale*, 2018, **10**, 22357–22361.
39 A. Campos, A. Arbouet, J. Martin, D. Gérard, J. Proust, J. Plain and M. Kociak, *ACS Photonics*, 2017, **4**, 1257–1263.
40 R. G. Hobbs, V. R. Manfrinato, Y. Yang, S. A. Goodman, L. Zhang, E. A. Stach and K. K. Berggren, *Nano Lett.*, 2016, **16**, 4149–4157.
41 J. Martin, M. Kociak, Z. Mahfoud, J. Proust, D. Gérard and J. Plain, *Nano Lett.*, 2014, **14**, 5517–5523.
42 E. D. Palik *Handbook of Optical Constants of Solids*, Academic press, 1998.
43 A. Losquin and M. Kociak, *ACS Photonics*, 2015, **2**, 1619–1627.
44 T. Coenen and A. Polman, *ACS Photonics*, 2019, **6**, 573–580.